Journal of the Chinese Society of Mechanical Engineers, Vol.46, No.6, pp669~678 (2025)

Investigation of Sloshing in a Sprayer Drone Tank with Blade-Shaped Baffles Using Numerical Simulations

Ahmet Mesut Ozturk* and Omer Gundogdu**

Keywords: CFD, Tank sloshing, Turbulence model, Water elevation.

ABSTRACT

The phenomenon of liquid sloshing affects the performance of UAVs used in agricultural spraying. The multi-directional sloshing forces that occur inside the tank can cause the drone to deviate from the specified route and collide with an obstacle. In this study, multiple blade-shaped baffles were used to suppress liquid sloshing in a sprayer drone tank. Numerical simulations using standard k-ε, standard k-ω, SST k-ω turbulence models were performed to evaluate effectiveness of this sloshing suppressor and compare it with a conventional suppressor. In these CFD simulations, the changes in total pressure, fluid velocity at a certain point in the tanks, sloshing force, and water elevation were examined for 50% and 65% filling ratios. It was demonstrated through numerical analyses that both suppressors were very effective in sloshing damping.

INTRODUCTION

The free surface movement that occurs in a tank partially filled with liquid under external excitation is called liquid sloshing. The hydrodynamic forces occurring within a tank due to sloshing may damage the tank or the supporting structure to which the tank is fixed. The extent of this damage depends on the fluctuations in the magnitude and distribution of the hydrodynamic forces that occur.

Paper Received December, 2024. Revised February, 2025. Accepted April, 2025. Author for Correspondence: Ahmet Mesut Ozturk.
E-mail: ahmetmesut.ozturk@ogr.atauni.edu.tr

** Ph.D. Student, Department of Mechanichal Engineering, Ataturk University, Erzurum 25240, Türkiye (0000-0003-0847-4895)*

*** Professor, Department of Mechanichal Engineering, Ataturk University, Erzurum 25240, Türkiye (0000-0003-2656-4181)*

Most of the studies conducted to date have focused on sloshing events occurring in large-sized tanks such as LNG tanks and aboveground liquid storage tanks. The most important reason for this is that any damage that may occur in such structures can cause loss of life and property. On the other hand, there are very few studies on liquid sloshing occurring in relatively smaller tanks, such as sprayer drone liquid tanks. It can be assumed that, with decreasing liquid volume, the extent of damage caused by sloshing will be less. However, this sloshing phenomenon may become a significant problem in precision agriculture practices. A violent sloshing movement that may occur within a sprayer drone tank may divert the drone from the previously determined route and reduce the efficiency of spraying. In addition, the drone, which deviates from its route due to liquid sloshing, may be damaged by hitting an obstacle. To prevent problems caused by sloshing, various sloshing suppression devices are employed.

Ahmed et al. (2022) proposed a flexible solution that can be used in sprayer drone tanks with different geometries. This solution was to use hollow balls made of PVC material. On the other hand, they conducted experimental comparison studies on various combinations of different types of tanks and baffles. As a result, it was determined that the hexagonal section tank was more effective in suppressing sloshing than the rectangular and cylindrical tank. It was also shown in their study that hollow plastic balls were more effective than vertical baffles.

Thirunavukkarasu and Rajagopal (2021) developed a configuration with horizontal and vertical baffles in their study. They named this configuration horivert baffle. They placed these baffle configurations in the variable mass region of the tank and performed sloshing analysis using CFD code. Before proceeding to the analysis phase, they conducted an experimental study in a tank without a suppressor in order to select the correct numerical model. As a result of this study, they chose to use the SST k-ω turbulence model. Pressure, velocity,

shear stress, and height of water in the tank were examined to evaluate the sloshing suppression performance of horivert baffle configurations. As a consequence, it was proven that the baffles with slots could suppress sloshing on the free surface of the liquid.

Zhang et al. (2019) evaluated the effectiveness of floating foams in suppressing sloshing using the results obtained from their experimental studies and the analytical potential flow solution they derived. As a result, it was observed that floating foams reduced both the sloshing amplitude and the dynamic pressure amplitude in a rectangular liquid tank, although the effectiveness of the foams varied with the number of foam layers used. Goudarzi and Danesh (2016) examined the sloshing phenomenon in a liquid storage tank under seismic excitation. Vertical baffles were used to suppress sloshing in this tank. They created an analytical model to predict the hydrodynamic damping effect caused by vertical baffles. Then, they created a numerical model based on the finite volume method and used this model to evaluate the accuracy of the analytical model.

Cho et al. (2017) stated that if the liquid sloshing frequency occurring in a swaying rectangular tank is equal to the resonance frequency, the tank walls may suffer structural damage. In order to prevent this situation and absorb the sloshing energy, they studied horizontal porous baffles. An analytical solution was obtained to evaluate sloshing suppression performance of these horizontal porous baffles. They applied MEEM (matched eigenfunction expansion method) to obtain this analytical solution. They also developed a numerical BEM (boundary element method) to verify the results obtained from MEEM. They proved that horizontal porous baffles attached to two opposite walls were more effective in suppressing sloshing in the tank, where sloshing occurred at the resonance frequency, compared to a single porous baffle placed in the center. Chu et al. (2018) focused on the sloshing phenomenon in a rectangular prism-shaped tank. They placed many baffles at regular intervals on the bottom of a water tank. They both conducted laboratory experiments and used a numerical method to investigate the effects of these baffles on the sloshing phenomenon. In laboratory studies, they excited the water in a rectangular tank using a shaking table. They used a Large Eddy Simulation (LES) model for the numerical method. They determined that if the number of baffles and the height of these baffles were increased, the hydrodynamic force and the maximum sloshing height decreased; otherwise, the effects of the baffles on the sloshing decreased.

Kim et al. (2018) emphasized that sloshing occurring at the resonance frequency can damage the structural parts of various systems operating under ocean conditions. In their work, they introduced the concept of moving baffles that contain a spring system, unlike conventional baffles. They conducted some experimental studies to evaluate the effectiveness of this concept in suppressing sloshing. In these experimental studies, baffles connected to two types of spring systems with different stiffnesses and a rectangular tank partially filled with liquid were used. Using images, pressure and force data obtained from sloshing experiments, the effectiveness of moving baffles in suppressing sloshing was examined.

Xue et al. (2017) investigated the effects of four different configurations of vertical baffles on impact pressure by conducting experiments under different forcing frequency values. It was observed that the vertical baffles used in the experiments changed the natural frequency and flow fields. It was also demonstrated that impact pressure could be effectively suppressed by using these vertical baffles. George and Cho (2020) examined the anti-slosh performance of a vertical baffle with many circular holes on it. They placed this vertical baffle in the center of a rolling rectangular liquid tank. They used the matched eigenfunction expansion method (MEEM), which incorporates an equivalent linearized quadratic loss model, to obtain an analytical solution to the current problem. On the other hand, they used incompressible unsteady Reynolds-averaged Navier-Stokes (RANS) equations containing a multiphase VOF model to obtain a numerical solution. To verify the results obtained from the analytical and numerical model, sloshing experiments were also carried out in a rectangular tank in rolling motion. In these experimental studies, the effects of the number of baffle pores and the submergence depth of the baffle on sloshing suppression were also investigated.

Xue et al. (2013) investigated the effects of two different types of baffles on sloshing through both experimental and numerical studies. The numerical results were obtained using a CFD code. They compared a conventional vertical baffle with a uniquely designed porous baffle under harmonic excitation. Upon examining the amplitude-frequency response curves, it was observed that the damping effect of the vertical baffle increased as the external excitation frequency decreased. In contrast, the damping effect of the porous baffle increased as the external excitation frequency increased. Kolaei et al. (2015) investigated the liquid sloshing in a horizontal cylindrical container with longitudinal baffles of different designs, using a coupled multimodal and boundary-element method. They examined the effects of baffle locations and dimensions on the natural slosh frequencies/modes, damping ratios, and hydrodynamic coefficients. Liu et al. (2018) investigated the effects of a ring baffle placed in an LNG tank on sloshing suppression by

considering the baffle's size and location parameters. The factors affecting the sloshing were selected as height (H), installation position (P), inclination angle (θ) and thickness (t). According to the results from CFD simulations, it was observed that the thickness parameter had minimal effect on sloshing. The height (H) parameter stood out as the most effective parameter. However, they observed that the effect of baffle height on sloshing suppression did not increase when the height exceeded 20% of the tank diameter.

Akyıldız et al. (2013) investigated the effects of ring baffles, placed in different arrangements, on sloshing in a rigid cylindrical tank through experimental studies. Experiments were repeated with different rolling angles, filling levels, and rolling frequencies. As a result, it was found that ring baffle configurations were highly effective in reducing the sloshing load. Maleki and Ziyaeifar (2008) investigated the potential of horizontal ring baffles and vertical blade baffles in damping hydrodynamic sloshing. They determined the hydrodynamic damping ratio of liquid sloshing in tanks using both experimental and analytical methods. As a result, they found that ring baffles are more effective in reducing sloshing oscillations in tanks subjected to horizontal excitation.

In this paper, the effectiveness of two different types of sloshing suppressors was evaluated in the liquid tank of a sprayer drone. One of these suppressors consists of four vertical ring baffles spaced at regular intervals. The other suppressor consists of two rows of vertical blade baffles arranged in opposite directions. These blade-shaped baffles have arc-shaped cross-sections, unlike the flat conventional vertical baffles. In most of the papers in the literature, flat vertical baffles with the same width as the tank are placed in a single row at the bottom. In the novel design presented in this paper, blade baffles are arranged in two rows at the bottom of the tank. To assess the sloshing suppression efficiency of these two types of suppressors, sloshing simulations were carried out using the finite volume method in hexagonal tanks with a width of 200 mm, a height of 180 mm, and a length of 260 mm. In the simulations, results were obtained for filling ratios of 50% and 65%. Mesh independence tests were performed in both a tank without any suppressors and in two other tanks containing the aforementioned suppressors to minimize the impact of the mesh structures of the fluid domains on the results. Since the results could vary depending on the flow model, the solutions were obtained using the standard k-ε, standard k-ω, and SST k-ω turbulence models in the numerical simulations. A uniaxial sloshing experiment was carried out to validate the flow model, and the water elevation amplitudes obtained from this experiment were compared with the results obtained from the numerical simulations. The tank without suppressors, the tank with ring baffles, and the tank with blade baffles of a unique design were all subjected to the same linear acceleration. These tanks were initially stationary, and after completing a one-second linear acceleration motion, their acceleration values were reduced to zero. Variations in horizontal sloshing force, water elevation, velocity magnitude, and total pressure were recorded for all the tanks during the numerical simulations.

NUMERICAL SIMULATIONS

In this section, three-dimensional models of the tank without suppressors, the tank with ring baffles, and the tank with uniquely designed blade baffles were first created using the SolidWorks program. Figures 1, 2, and 3 show the dimensions of the tanks. All tanks used in the numerical simulations have identical geometric dimensions.

In order to avoid wordiness, the following abbreviations are used for the 3D models of the tanks in the remaining part of the study:

- Tank 1 refers to the tank model without any sloshing suppressor.
- Tank 2 refers to the tank model containing four vertical ring baffles placed at specific intervals.
- Tank 3 refers to the tank model containing two rows of vertical blade baffles arranged in opposite directions.

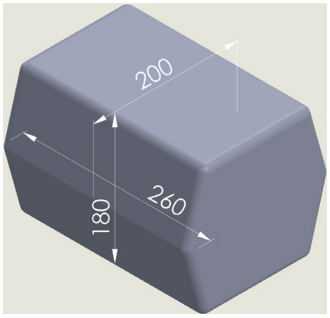

Fig. 1. Dimensions of Tank 1 (all dimensions are in mm).

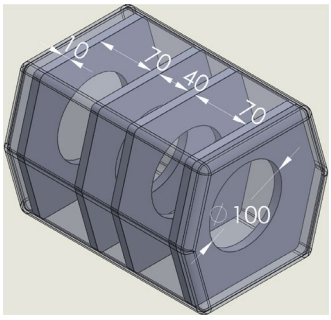

Fig. 2. Dimensions of Tank 2 (all dimensions are in mm).

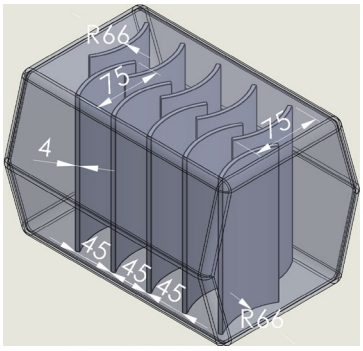

Fig. 3. Dimensions of Tank 3 (all dimensions are in mm).

The Fluid Flow (Fluent) system in the ANSYS program was used to simulate the sloshing phenomenon in the tanks. First of all, the tank models were transferred separately into the geometry cells in the Fluent system. Then, the geometric boundaries of the fluid volumes in the tanks were determined. Figure 4 presents the total fluid volume for Tank 1 with a 50% filling ratio. The physical properties of the fluids used in the simulations are presented in Table 1.

Table 1. The physical properties of the fluids used in the numerical simulations.

The physical properties of fluids	Air	Water (liquid)
Density (kg/m^3)	1.225	998.2
Viscosity (kg/(m.s))	1.7894e-05	0.001003

Sensors, whose coordinates are shown in Figure 4, were used to monitor the fluid velocity and pressure in the tanks. The positions of the sensors remained constant in all the sloshing simulations.

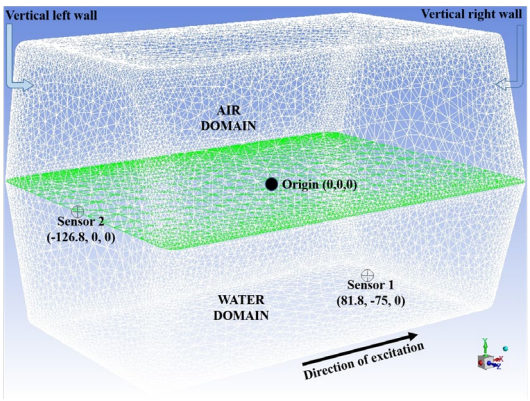

Fig. 4. The sensor coordinates (all dimensions are in mm).

Mesh generation and validation

After the fluid volumes of the tank models were created, the mesh structures were generated so that the flow-related equations could be solved. The total fluid volumes of the tanks were divided into tetrahedral finite elements, each with four nodes. For example, the mesh structure generated for the total fluid volume of Tank 1 is represented in Figure 5.

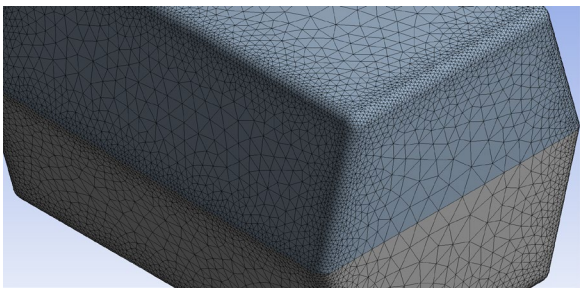

Fig. 5. The mesh structure generated for the total fluid volume of Tank 1.

The mesh structure generated for the total fluid volume of Tank 1 contains 45791 nodes and 231760 elements. However, the number of nodes and elements must be sufficient to solve the problem with high accuracy. Mesh independence tests were performed to minimize the impact of the mesh structures on the results. Three different mesh sizes were used for the tank models in these tests. For each mesh size, the total pressure was measured at the location of Sensor 1. Total pressure measurements were taken while the fluids inside the tanks were at rest. Details of the mesh independence tests are presented in Table 2.

Table 2. Details of the mesh independence tests.

Tanks	Mesh size number	Number of nodes	Number of elements	Total pressure (Pa)
Tank 1	1	12021	64896	752.4357
Tank 1	2	23107	126946	736.2046
Tank 1	3	45791	231760	733.9294
Tank 2	1	13695	68038	715.9714
Tank 2	2	26940	138787	736.5500
Tank 2	3	44777	213600	741.2552
Tank 3	1	15443	74465	716.5431
Tank 3	2	27586	137548	737.2281
Tank 3	3	52414	257579	740.9557

Kalidas et al. (2023) stated that the refinement ratio between mesh sizes in the mesh independence test should be greater than 1.3. The refinement ratio between the number of elements of mesh sizes 1 and 2 of Tank 1 is 1.96. The refinement ratio between the element numbers of the second and third mesh sizes is 1.83. The percentage difference between the total pressure values for the first and second mesh sizes is 2.16%. The percentage difference between the total pressure values for the second and third mesh sizes is 0.31%. This difference is below 1%.

To obtain a high-accuracy solution, the third mesh size, consisting of 231760 elements, was selected for Tank 1. The refinement ratio between the number of elements of mesh sizes 1 and 2 of Tank 2 is 2.04. The refinement ratio between the element numbers of the second and third mesh sizes is 1.54. The percentage difference between the total pressure values for the first and second mesh sizes is 2.87%. The percentage difference between the total pressure values for the second and third mesh sizes is 0.64%. The third mesh size, consisting of 213600 elements, was selected for Tank 2. The refinement ratio between the number of elements of mesh sizes 1 and 2 of Tank 3 is 1.85. The refinement ratio between the element numbers of the second and third mesh sizes is 1.87. The percentage difference between the total pressure values for the first and second mesh sizes is 2.89%. The percentage difference between the total pressure values for the second and third mesh sizes is 0.5%. The third mesh size, consisting of 257579 elements, was selected for Tank 3.

Modeling and solution techniques for turbulent flow in the tanks

Since air and water in the tanks do not mix, the movements of these fluids can be examined using the VOF model. Therefore, time-dependent solutions for the air-water interface were obtained during sloshing in the tanks using the VOF model.

In this numerical study, mass conservation, momentum conservation and energy conservation equations were solved to simulate the sloshing phenomenon, using the finite volume method. The mass conservation equation can be described as follows:

$$\frac{\partial \rho}{\partial t} + \frac{\partial (\rho u_i)}{\partial x_i} = 0 \quad (1)$$

where t represents the time, u is the velocity, ρ is the density of the liquid, i represents the direction, x_i is the coordinate in the i direction. The momentum conservation equation can be described as follows:

$$\frac{\partial (\rho u_i)}{\partial t} + \frac{\partial (\rho u_i u_j)}{\partial x_i} = -\frac{\partial p}{\partial x_i} + \frac{\partial \tau_{ij}}{\partial x_i} + \rho g_i + F_i \quad (2)$$

where p is the pressure, g is the gravitational acceleration, τ_{ij} is the stress tensor, F_i is the other energy term.

Because the sloshing flow in the tanks is in a turbulent state, the system must also comply with the turbulent transport equations. The standard k-ε model is based on the equations governing turbulence kinetic energy (k) and the turbulence dissipation rate (ε):

$$\frac{\partial (\rho k)}{\partial t} + \frac{\partial (\rho k u_i)}{\partial x_i} = \frac{\partial}{\partial x_j}\left[\left(\mu + \frac{\mu_t}{\sigma_k}\right)\frac{\partial k}{\partial x_j}\right] + G_k - \rho\varepsilon \quad (3)$$

$$\frac{\partial (\rho \varepsilon)}{\partial t} + \frac{\partial (\rho \varepsilon u_i)}{\partial x_i} = \frac{\partial}{\partial x_j}\left[\left(\mu + \frac{\mu_t}{\sigma_\varepsilon}\right)\frac{\partial \varepsilon}{\partial x_j}\right] + \frac{C_{1\varepsilon}}{k} G_k - C_{2\varepsilon}\rho\frac{\varepsilon^2}{k} \quad (4)$$

$$\mu_t = \frac{\rho C_\mu k^2}{\varepsilon} \quad (5)$$

$$G_k = \mu_t \left(\frac{\partial u_i}{\partial x_j} + \frac{\partial u_j}{\partial x_i}\right)\frac{\partial u_i}{\partial x_j} \quad (6)$$

where μ is the laminar viscosity coefficient, μ_t is the turbulent viscosity coefficient, G_k is the generation term of turbulence kinetic energy (k) due to the mean velocity gradient. In k-ω models, the transport equation for the turbulent dissipation rate (ε) is replaced with an equation for the specific dissipation rate (ω). The SST k-ω model is a variant of the standard k-ω model. This turbulence model combines the original Wilcox's k-ω model, used to model flow near solid surfaces, and the standard k-ε model, used to model flow away from solid surfaces. During the simulations, the water elevation on the right-side wall of the tanks was recorded using these turbulence models.

In the numerical simulations, the total simulation time was partitioned into time steps of 0.004 seconds. Each time step was iterated for 20 cycles to ensure that the absolute convergence criterion of 0.001 was met. At the beginning of the simulations, the solutions for the stationary states of the tanks were obtained for 0.5 seconds. Then, all the tanks were forced to move linearly in the +X direction with an acceleration of 2 m/s² for one second. At the end of this accelerated movement, the acceleration was set to 0 m/s², and the course of the sloshing event was monitored. In this way, it was simulated that the sloshing in the sprayer drone's tank started with a sudden acceleration and ended over time after the drone reached a constant speed. The excitation condition, considered for both the numerical simulations and the uniaxial sloshing experiment, is presented in Figure 6.

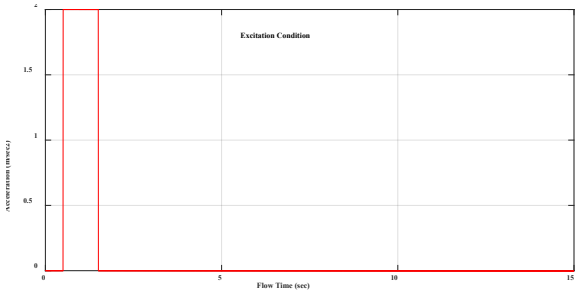

Fig. 6. The excitation condition.

Model verification and validation

In this part of the study, the numerical results obtained under the excitation condition presented in Figure 6 for a tank with a 50% filling ratio and no sloshing suppressor were verified with the experimental results. A tank without a suppressor was

manufactured using a 3D printer with transparent PLA filament. A linear motion system was established to experimentally monitor the sloshing in the manufactured tank. This linear motion system is presented in Figure 7.

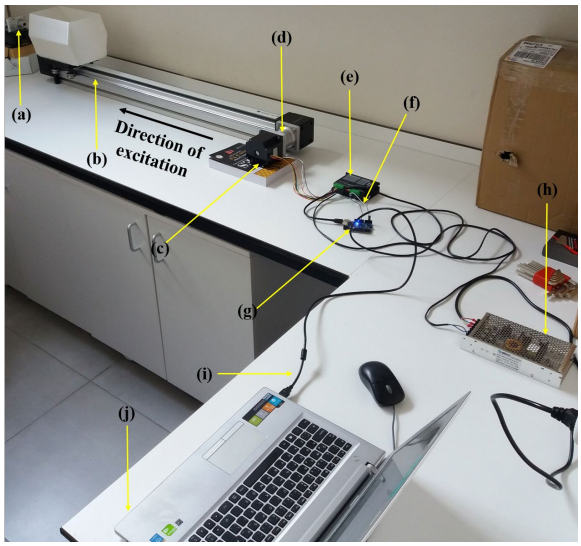

Fig. 7. The linear motion system. (a) Video camera; (b) Linear slide; (c) Stepper motor; (d) Coupling pair (Flange + Coupling); (e) Stepper motor driver; (f) Jumper cables; (g) Microcontroller card; (h) Power supply; (i) USB cable; (j) Notebook.

In the sloshing test performed on the linear slide, a camera was used to track and record the maximum elevation of the water level on the tank's vertical wall. Amplitudes were obtained from the recorded images using the scaling and object transformation tools in the SolidWorks software. The positive amplitude measured at 3.5 seconds and the negative amplitude measured at 7.1 seconds are presented in Figures 8 and 9, respectively.

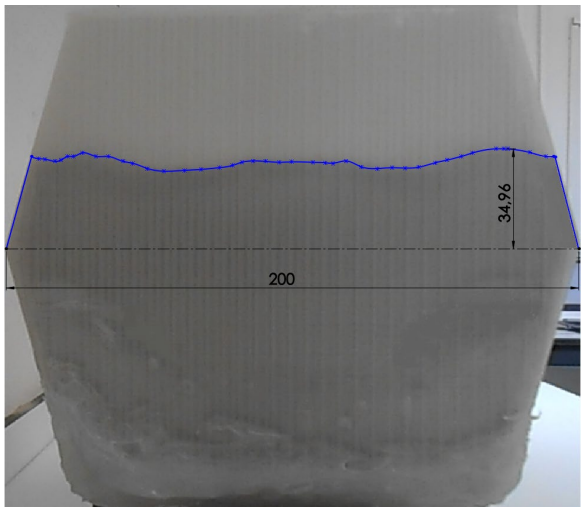

Fig. 8. The positive amplitude measured at 3.5 seconds (all dimensions are in mm).

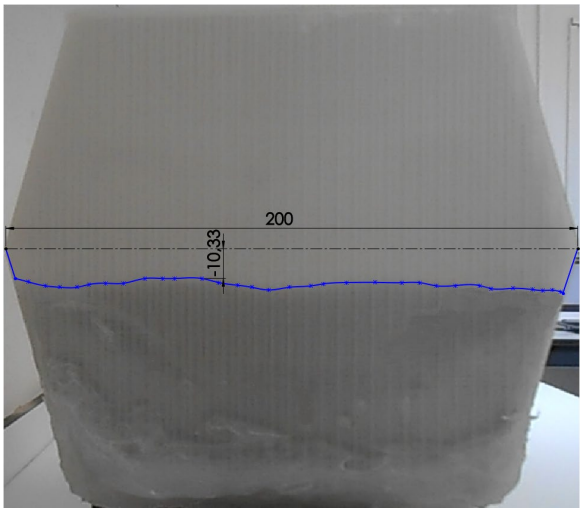

Fig. 9. The negative amplitude measured at 7.1 seconds (all dimensions are in mm).

The amplitude values obtained from the experimental images recorded at different durations are presented in Figure 10, along with the water elevation values obtained from the numerical simulations for the tank without a suppressor. The standard k-ω turbulence model was found to be more suitable in predicting the sloshing phenomenon in the tank without a suppressor. For this reason, the standard k-ω turbulence model was used in all the numerical simulations for the remainder of the study.

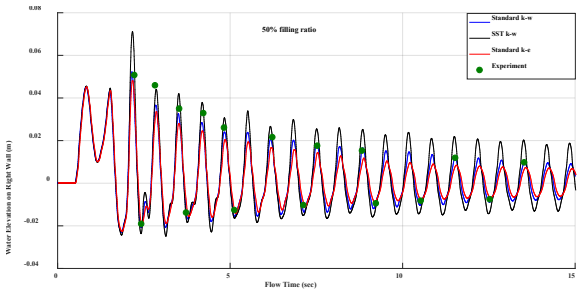

Fig. 10. The water elevation-flow time graph for the tank without a suppressor.

RESULTS AND DISCUSSIONS

Analysis of the total pressure-flow time graphs obtained from the numerical simulations

In this part of the study, the effects of different types of sloshing suppressors on the total pressure in the tanks were examined and compared. The pressure variations recorded by Sensor 2 in the tanks are shown in Figs. 11-12. In all the pressure-time graphs, it can be seen that the water in the tanks initially remained motionless for 0.5 seconds. During this period, the pressure values remained constant in all the tanks. Then, the tanks were forced

to make a linear movement with an acceleration of 2 m/s² for one second. Under the influence of this accelerated movement, fluctuations occurred in the pressure values. In the remaining time, the acceleration was reduced to 0 m/s² in all the simulations, and the pressure values were expected to return to their stationary state values.

When the total pressure-flow time graph in Fig. 11, obtained at a 50% filling ratio, is examined, it can be observed that the pressure in Tank 1 reaches a maximum value of 234.1 Pa. The lowest pressure amplitude value measured at the end of the simulation period in Tank 1 was 67.67 Pa. All pressure amplitude values measured in Tank 1 before the 9.848th second remained above 100 Pa. Figure 11 shows that the maximum total pressure value measured in Tank 2 was 44.82 Pa. The pressure amplitude values in Tank 2 dropped below 1 Pa after 8.136 seconds. Figure 11 also shows that the highest pressure amplitude value measured in Tank 3 was 95.07 Pa. The lowest total pressure amplitude value measured at 14.58 seconds in Tank 3 was 1.316 Pa.

When the total pressure-flow time graph in Fig. 12, obtained at a 65% filling ratio, is examined, it can be observed that the pressure in Tank 1 reaches a maximum amplitude of 203.8 Pa. The lowest pressure amplitude value measured at the end of the simulation period in Tank 1 was 60 Pa. Figure 12 shows that the maximum amplitude measured in Tank 2 was 96.7 Pa. The lowest total pressure amplitude measured at 14.66 seconds in Tank 2 was 7.9 Pa. Figure 12 also shows that the highest pressure amplitude measured in Tank 3 was 117.5 Pa. The lowest amplitude measured at 14.91 seconds in Tank 3 was 9.3 Pa.

Considering the total pressure data, the highest pressure values in both graphs obtained at different filling ratios were observed in Tank 1, Tank 3, and Tank 2, respectively. The pressure amplitudes in Tank 2 and Tank 3 were largely suppressed after about the 5th second in the graph obtained at a 50% filling ratio. The pressure amplitude values measured in Tank 1 remained considerably higher than those in Tanks 2 and 3 in both graphs obtained at different filling ratios. This is because the ring and blade baffles significantly reduce the fluid movement and therefore reduce the impact pressure acting on Sensor 2 located on the tank wall. However, when the pressure data obtained at a 65% filling ratio were examined, a slight decrease in the suppression performance of the ring and blade baffles was observed. The increase in the filling ratio caused an increase in the amplitude and frequency of the pressure waves in Tanks 2 and 3. Although both suppressors were effective in damping the sloshing, the pressure values did not stabilize completely.

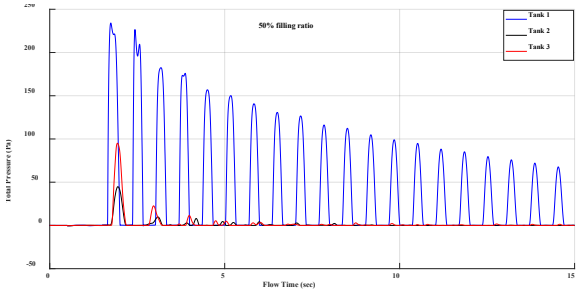

Fig. 11. The total pressure-flow time graph obtained at a 50% filling ratio.

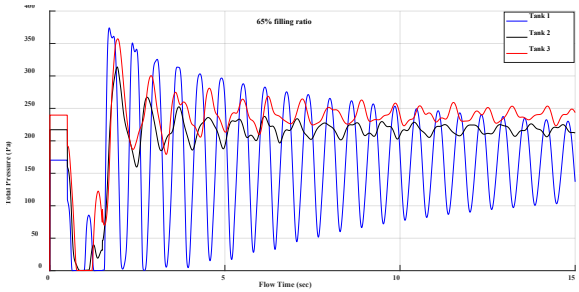

Fig. 12. The total pressure-flow time graph obtained at a 65% filling ratio.

Analysis of the velocity magnitude-flow time graphs obtained from the numerical simulations

In this section, the velocity variations that occur during sloshing in the tanks are examined. Examining the velocity magnitude-flow time graphs in Figs. 13-14, we can observe that there is no variation during the first 0.5 seconds. The velocity values measured by Sensor 2 during this period are 0 m/s. When the tanks are subjected to an accelerated movement for one second, it is seen that the velocity values begin to fluctuate. After this excitation, which lasts for one second, ends, it is seen that the velocity amplitude values tend to decrease until the end of the simulation period.

When the velocity magnitude-flow time graph in Fig. 13, obtained at a 50% filling ratio, is examined, it is seen that the maximum velocity in Tank 1 is 0.4 m/s. In Tank 1, the velocity amplitude values dropped below 0.15 m/s after 7.728 seconds. The velocity amplitude value measured at 14.7 seconds in Tank 1 is 0.094 m/s. Figure 13 shows that the maximum speed value measured in Tank 2 is 0.1452 m/s. In Tank 2, the velocity amplitude values dropped below 0.02 m/s after 10.41 seconds. Figure 13 also shows that the maximum velocity value measured in Tank 3 is 0.1393 m/s. The lowest velocity amplitude value in Tank 3 was measured as 0.028 m/s at 14.51 seconds.

When the velocity magnitude-flow time graph in Fig. 14, obtained at a 65% filling ratio, is examined, it is seen that the maximum velocity in

Tank 1 is 0.4 m/s. In Tank 1, the velocity amplitude values dropped below 0.15 m/s after 5.068 seconds. The velocity amplitude measured at 14.95 seconds in Tank 1 is 0.069 m/s. Figure 14 shows that the maximum velocity measured in Tank 2 is 0.1694 m/s. In Tank 2, the velocity amplitude values dropped below 0.05 m/s after 2.048 seconds. Figure 14 also shows that the maximum velocity measured in Tank 3 is 0.2252 m/s. In Tank 3, the velocity amplitude values dropped below 0.05 m/s after 4.44 seconds.

In both graphs obtained at different filling ratios, the maximum velocity magnitude values measured in Tank 2 and Tank 3 are close to each other and are much lower than those in Tank 1. In the graph, obtained at a 50% filling ratio, if 0.05 m/s is used as the reference value, the time required for the velocity amplitude values in Tank 3 to decrease to the minimum is approximately 0.5 sec longer than the time required in Tank 2. The time required increased to 2.4 seconds in the graph obtained at a 65% filling ratio. The velocity amplitude values measured in Tank 1 remained above 0.05 m/s throughout the simulation periods in both graphs, which were obtained at different filling ratios. As is known, rigid obstacles in the liquid flow can create vortices due to their sharp edges. These vortices and the resulting turbulence can also reduce the velocity of the liquid and, therefore, its energy. For this reason, dissipation of the sloshing energy in Tank 1 takes longer than in Tanks 2 and 3.

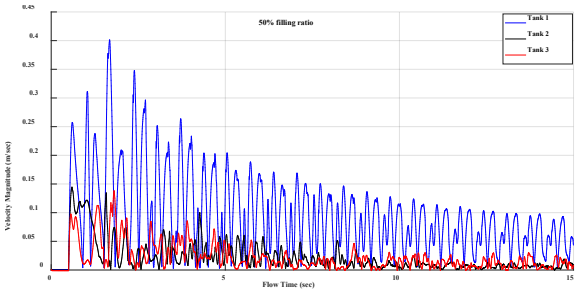

Fig. 13. The velocity magnitude-flow time graph obtained at a 50% filling ratio.

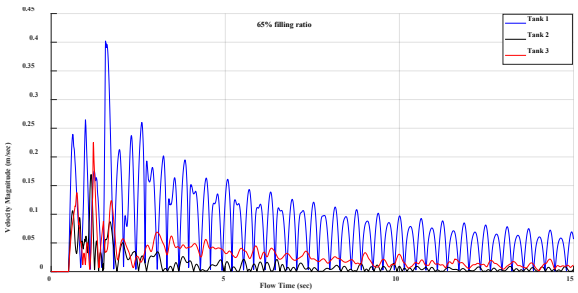

Fig. 14. The velocity magnitude-flow time graph obtained at a 65% filling ratio.

Analysis of the sloshing force-flow time graphs obtained from the numerical simulations

In this section, sloshing force variations that occur as a result of excitation in the tanks is examined. The variation in the sloshing force occurring in the direction of the excitation shown in Figure 4, on the X axis, was recorded during the numerical simulations for all the tanks.

When the sloshing force-flow time graph in Fig. 15, obtained at a 50% filling ratio, is examined, it is seen that the highest sloshing force measured in the direction of excitation in Tank 1 was 10.95 N. The lowest sloshing force amplitude measured at the end of the simulation period in Tank 1 was 2.06 N. Figure 15 shows that the highest sloshing force value measured in Tank 2 was 7.27 N. The sloshing force amplitude in Tank 2 decreased to 0.469 N at 2.412 seconds. In Tank 2, the sloshing force amplitudes dropped below 0.1 N after 11.55 seconds. Figure 15 also shows that the highest sloshing force value measured in Tank 3 was 7.927 N. In Tank 3, the sloshing force amplitude decreased to 0.6115 N at 2.444 seconds. In Tank 3, the sloshing force amplitudes dropped below 0.1 N after 10.38 seconds.

When the sloshing force-flow time graph in Fig. 16, obtained at a 65% filling ratio, is examined, it is seen that the highest sloshing force measured in the direction of excitation in Tank 1 was 13.18 N. The lowest sloshing force amplitude measured at the end of the simulation period in Tank 1 was 1.89 N. Figure 16 shows that the highest sloshing force measured in Tank 2 was 9.3 N. The sloshing force amplitude in Tank 2 decreased to 0.822 N at 2.36 seconds. The lowest amplitude measured at 14.19 seconds in Tank 2 was 0.142 N. Figure 16 also shows that the highest sloshing force value measured in Tank 3 was 10.08 N. In Tank 3, the sloshing force amplitude decreased to 0.868 N at 2.4 seconds. The lowest amplitude measured at 14.57 seconds in Tank 3 was 0.141 N.

In contrast to the effective sloshing damping observed in Tanks 2 and 3, the sloshing force amplitudes in Tank 1 did not fall below 1.89 N in both graphs. Both the direction of the hydrodynamic force component generated in the direction of excitation during sloshing were changed by the ring and blade baffles, and their magnitude was reduced by the ring and blade baffles. In both graphs obtained at different filling ratios, the maximum sloshing force is approximately 34% lower in Tank 2 and approximately 28% lower in Tank 3 compared to Tank 1. Although ring baffles were relatively more successful in reducing the maximum sloshing force, blade and ring baffles showed similar performance when their overall sloshing force suppression was considered.

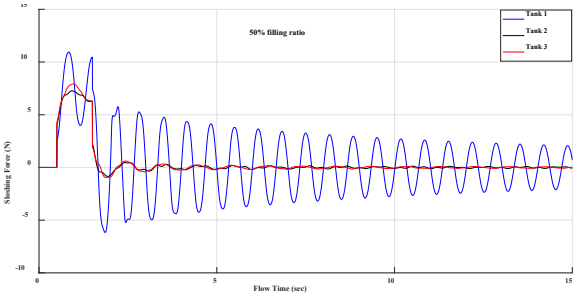

Fig. 15. The sloshing force-flow time graph obtained at a 50% filling ratio.

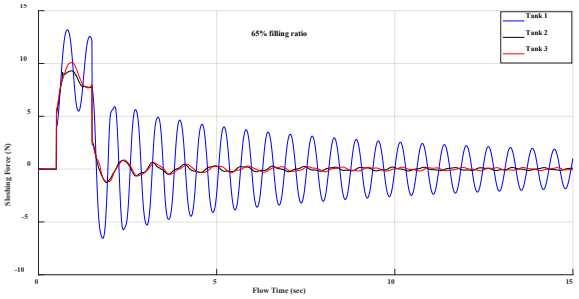

Fig. 16. The sloshing force-flow time graph obtained at a 65% filling ratio.

Analysis of the water elevation-flow time graphs obtained from the numerical simulations

In this section, water elevation measurements were taken for all the tanks. The elevation values that the top point of the water could reach on the vertical right walls of the tanks were measured. The water elevation-flow time graphs obtained at different filling ratios are presented in Figs. 17-18.

When the water elevation-flow time graph in Fig. 17, obtained at a 50% filling ratio, is examined, it is seen that the maximum water elevation measured in Tank 1 was 52.25 mm. The water elevation amplitude measured at 14.87 seconds in Tank 1 was 9.178 mm. Figure 17 shows that the maximum water elevation measured in Tank 2 was 34.92 mm. The water elevation amplitude measured at 2.568 seconds in Tank 2 was 5.713 mm. In Tank 2, the water elevation amplitudes dropped below 2 mm after 4.648 seconds. Figure 17 also shows that the maximum water elevation measured in Tank 3 was 40.3 mm. The water elevation amplitude measured at 2.452 seconds in Tank 3 was 7.931 mm. In Tank 3, the water elevation amplitudes dropped below 2 mm after 12.17 seconds.

When the water elevation-flow time graph in Fig. 18, obtained at a 65% filling ratio, is examined, it is seen that the maximum amplitude measured in Tank 1 was 48.8 mm. The water elevation amplitude measured at 14.49 seconds in Tank 1 was 8.5 mm. Figure 18 shows that the maximum amplitude measured in Tank 2 was 32.5 mm. The water elevation amplitude measured at 3.2 seconds in Tank 2 was 9.8 mm. The water elevation amplitude measured at 14.24 seconds in Tank 2 was 0.2 mm. Figure 18 also shows that the maximum amplitude measured in Tank 3 was 41.9 mm. The water elevation amplitude measured at 3.37 seconds in Tank 3 was 6.1 mm. The water elevation amplitude measured at 14.71 seconds in Tank 3 was 1.4 mm.

In both graphs obtained at different filling ratios, the maximum water elevation in Tank 2 is approximately 33% lower than that in Tank 1. Depending on filling ratios, the maximum water elevation in Tank 3 is between 14% and 23% lower than that in Tank 1. On the other hand, when the water elevation amplitudes around the 2.5-second mark are considered in the graph obtained at a 50% filling ratio, it can be seen that the amplitude measured in Tank 1 remains above 36 mm. At the given moment in this graph, it is observed that the amplitudes in Tanks 2 and 3 fell below 8 mm. As a result, although ring baffles were more successful than blade baffles in reducing the maximum sloshing elevation, both types of baffles exhibited a similar sloshing damping pattern over the entire simulation period, as well as in suppressing the sloshing force.

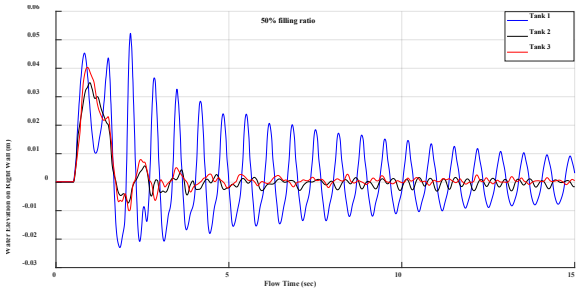

Fig. 17. The water elevation-flow time graph obtained at a 50% filling ratio.

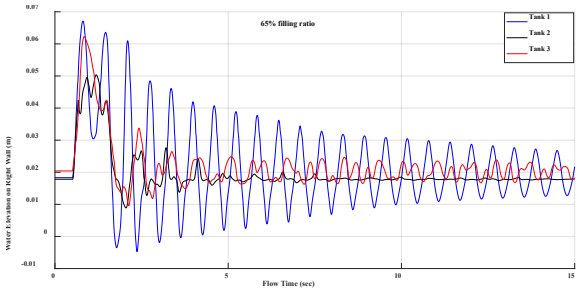

Fig. 18. The water elevation-flow time graph obtained at a 65% filling ratio.

CONCLUSIONS

In this paper, a sloshing suppressor consisting of multiple blade-shaped baffles was presented. This passive suppressor, which is designed for the liquid tanks of sprayer drones, has a unique geometry. In the paper, the sloshing suppression

performance of this passive suppressor was compared with that of ring baffles, which were widely preferred in LNG tanks. This comparison was carried out by sloshing simulations conducted in hexagonal tanks using ANSYS Fluent. According to the simulation results, findings demonstrate the effectiveness of baffles in stabilizing the liquid within the tank. Although ring baffles were more successful than blade baffles in reducing the amplitudes in all observed parameters, it was noted that the sloshing damping patterns of the blade-shaped baffles and the ring baffles were quite similar across all the graphs showing changes in total pressure, velocity magnitude, sloshing force, and water elevation parameters. In conclusion, the blade baffles introduced in the paper can be effectively used in a hexagonal drone tank. However, additional studies, such as dimension optimization, are required to prevent the decrease in suppression performance of the blade baffles caused by the increase in the filling ratio. Among the two designs, the ring baffles exhibit superior suppression performance, achieving the fastest attenuation of sloshing, whereas the blade-shaped baffles offer a novel structural configuration adaptable to different tank geometries. This study confirms that both baffle types significantly enhance UAV operational precision and safety. Additionally, the proposed designs hold potential for broader applications, including fuel transportation tanks, LNG storage systems, and other fluid containment structures, where improved sloshing suppression can enhance stability and performance.

ACKNOWLEDGMENT

This research study was supported by the Scientific Research Projects Coordination Unit of Ataturk University in Turkey. The code number of the research project supported by this institution is FDK-2022-11110.

REFERENCES

Ahmed, S., Xin, H., Faheem, M. & Qiu, B., 2022. "Stability analysis of a sprayer UAV with a liquid tank with different outer shapes and inner structures." *Agriculture*, 12, p. 379.

Akyıldız, H., Ünal, N.E. and Aksoy, H., 2013. An experimental investigation of the effects of the ring baffles on liquid sloshing in a rigid cylindrical tank. *Ocean Engineering*, 59, pp.190-197.

Cho, I., Choi, J.S. & Kim, M., 2017. "Sloshing reduction in a swaying rectangular tank by a horizontal porous baffle." *Ocean Engineering*, 138, pp. 23-34.

Chu, C.R., Wu, Y.R., Wu, T.R. & Wang, C.Y., 2018. "Slosh-induced hydrodynamic force in a water tank with multiple baffles." *Ocean Engineering*, 167, pp. 282-292.

George, A. & Cho, I., 2020. "Anti-sloshing effects of a vertical porous baffle in a rolling rectangular tank." *Ocean Engineering*, 214, p. 107871.

Goudarzi, M.A. & Danesh, P.N., 2016. "Numerical investigation of a vertically baffled rectangular tank under seismic excitation." *Journal of Fluids and Structures*, 61, pp. 450-460.

Kalidas, S., Rangasamy, R. & Seenivasan, V., 2023. "Investigation on the 1-kW Francis turbine elbow type draft tube performance by numerical and optimisation approach." *Progress in Computational Fluid Dynamics, an International Journal*, 23(1), pp. 24-33.

Kim, S.P., Chung, S.M., Shin, W.J., Cho, D.S. & Park, J.C., 2018. "Experimental study on sloshing reduction effects of baffles linked to a spring system." *Ocean Engineering*, 170, pp. 136-147.

Kolaei, A., Rakheja, S. and Richard, M.J., 2015. "A coupled multimodal and boundary-element method for analysis of anti-slosh effectiveness of partial baffles in a partly-filled container." *Computers & Fluids*, 107, pp.43-58.

Liu, G., Lin, Y., Guan, G. and Yu, Y.Y., 2018. "Numerical research on the anti-sloshing effect of a ring baffle in an independent type C LNG tank." *Journal of Zhejiang University-Science A*, 19(10), pp.758-773.

Maleki, A. & Ziyaeifar, M., 2008. "Sloshing damping in cylindrical liquid storage tanks with baffles." *Journal of Sound and Vibration*, 311(1-2), pp. 372-385.

Thirunavukkarasu, B. & Rajagopal, T.K.R., 2021. "Numerical investigation of sloshing in tank with horivert baffles under resonant excitation using CFD code." *Thin-Walled Structures*, 161, p. 107517.

Xue, M.A., Lin, P.Z., Zheng, J.H., Ma, Y.X., Yuan, X.L. and Nguyen, V.T., 2013. "Effects of perforated baffle on reducing sloshing in rectangular tank: experimental and numerical study." *China Ocean Engineering*, 27(5), pp.615-628.

Xue, M.A., Zheng, J., Lin, P. & Yuan, X., 2017. "Experimental study on vertical baffles of different configurations in suppressing sloshing pressure." *Ocean Engineering*, 136, pp. 178-189.

Zhang, C., Su, P. & Ning, D., 2019. "Hydrodynamic study of an anti-sloshing technique using floating foams." *Ocean Engineering*, 175, pp. 62-70.